Determination of Carrier Density and Dynamics via Magnetoelectroluminescence Spectroscopy in Resonant-Tunneling Diodes

E.R. Cardozo de Oliveira,[1] A. Naranjo,[1] A. Pfenning,[2,*] V. Lopez-Richard,[1] G.E. Marques,[1] L. Worschech,[2] F. Hartmann,[2,†] S. Höfling,[2] and M.D. Teodoro[1]

[1] *Departamento de Física, Universidade Federal de São Carlos, São Carlos, São Paulo 13565-905, Brazil*

[2] *Technische Physik, Physikalisches Institut and Röntgen Center for Complex Material Systems (RCCM), Universität Würzburg, Am Hubland, Würzburg D-97074, Germany*

(Received 23 July 2020; revised 7 September 2020; accepted 18 December 2020; published 22 January 2021)

We study the magneto-transport and magnetoelectroluminescence properties of purely *n*-doped GaAs/$Al_{0.6}Ga_{0.4}As$ resonant-tunneling diodes with an $In_{0.15}Ga_{0.85}As$ quantum well and an emitter prewell. Before the resonant-current condition, magneto-transport measurements reveal charge-carrier densities comparable for diodes with and without the emitter prewell. Landau-level splitting is observed in the electroluminescence emission from the emitter prewell, enabling the determination of the charge-carrier buildup. Our findings show that magnetoelectroluminescence spectroscopy techniques provide useful insights into the charge-carrier dynamics in resonant-tunneling diodes and comprise a versatile tool to complement magneto-transport techniques. This approach might pave the way for the development of potentially more efficient optoelectronic resonant-tunneling devices by, e.g., monitoring voltage-dependent charge accumulation for the improvement of built-in fields and hence the maximization of the photodetector efficiency and/or the minimization of optical losses.

DOI: 10.1103/PhysRevApplied.15.014042

I. INTRODUCTION

Resonant-tunneling diodes (RTDs), with their current peak followed by a region of negative differential conductance (NDC) [1–3], are semiconductor devices with potential applications as terahertz oscillators [4,5], fast switches [6], and optically active elements in optoelectronic circuits [7,8] and photodetectors [9–12]. The charge-carrier dynamics rule their functionalities and detection abilities. Given that charge excitation, accumulation, and transport control the device operational parameters and responsivity, it is important to study how all these three properties are combined.

Charge carriers can be generated optically or injected by an applied voltage and the RTD response is affected by the way in which they are collected and stored. Magneto-transport measurements have become well-settled means of studying space-charge buildup in RTDs, as described in Refs. [13–17]. However, as demonstrated in this work, blind spots can emerge where the magneto-transport tools are unable to provide a complete characterization of the charge-accumulation scheme within the main operational range of the device. Under such circumstances, it is necessary to appeal to a combination of both transport and optical observations, as set out in the following discussion.

The insertion of an emitter prewell adjacent to the double barrier has proven to be a relevant design ingredient to study charge-carrier accumulation [18–23]. It improves the peak current density and the peak-to-valley current ratio (PVCR) at room temperature by suppressing states above the prewell, increasing the charge-carrier density close to the emitter barrier and increasing the overlap of localized states in the prewell and quasibound states in the double-barrier quantum well (DBQW) [18,20,21]. In the case presented in this paper, the ability to clearly resolve the Landau quantization of the electroluminescence (EL) emission from states confined in the prewell has been crucial. The resolution attained for this observation allows characterization of the filling of levels and, subsequently, the charge accumulation. In order to do that, one must first clearly ascribe each emission line to the correct site at the RTD where the optical recombination occurs. In this sense, given the band structure tuning along the heterolayered system, spectroscopic tools are better suited for the charge-buildup mapping along the growth direction. This is an advantage over just transport characterizations, where the overlap of various simultaneous channels cannot be deconvoluted, unlike the case of the clearly resolved emission lines of the optical spectrum [13,14,24]. In unipolar doped RTDs, as is the case under consideration here, EL

*andreas.pfenning@physik.uni-wuerzburg.de
†fabian.hartmann@physik.uni-wuerzburg.de

appears by combining high electric fields in the lightly doped absorption region with the relatively small gap that controls the impact-ionization threshold [25–28] or, potentially, the Zener tunneling [29]. Thus, we can take advantage of the emitted light to investigate the charge-carrier dynamics via a combination of both magneto-EL and magneto-transport. The subject of magneto-transport has been studied extensively in the 1990s and most works report the magneto-optic response through photoluminescence (PL). In this sense, we propose a complete investigation by complementing the transport properties and the intrinsic EL response along with the PL to describe the charge-carrier dynamics in n-doped – intrinsic – n-doped (*n-i-n*) GaAs/$Al_{0.6}Ga_{0.4}As$ resonant-tunneling diodes with $In_{0.15}Ga_{0.85}As$ emitter prewells and compare the results with a conventional GaAs/AlGaAs RTD reference sample without a prewell.

As charge accumulation is the paramount working mechanism in RTD photodetectors, this approach for investigating these heterostructures may contribute to the development of potentially more efficient optoelectronic resonant-tunneling devices by, e.g., monitoring voltage-dependent charge accumulation for the improvement of built-in fields and hence the maximization of the photodetector efficiency and/or the minimization of optical losses.

II. SAMPLE DESIGN AND EXPERIMENTAL SETUP

A. Synthesis and structural characterization

Two samples are grown by molecular-beam epitaxy. The first heterostructure consists of an intrinsic GaAs/$Al_{0.6}Ga_{0.4}As$ double-barrier structure (DBS), followed by a lightly doped ($n \approx 10^{17}$ cm^{-3}) 100-nm-thick GaAs drift region and a highly doped ($n \approx 10^{18}$ cm^{-3}) $Al_{0.2}Ga_{0.8}As$ optical window. The growth details can be found in Ref. [25]. The InGaAs sample differs in just the intrinsic region, where a 5-nm and 4-nm $In_{0.15}Ga_{0.85}As$ prewell and quantum well, respectively, are introduced. The sample with the InGaAs prewell and quantum well is labeled as S-InGaAs and the GaAs/AlGaAs RTD, used as a reference, is labeled as Ref-GaAs. The layout and structural properties of the S-InGaAs RTD are shown in Fig. 1. A cross-section scanning-electron-microscopy (SEM) image of the S-InGaAs RTD is displayed in Fig. 1(a). Well-defined interfaces can be observed. An enlargement of the DBS (inset) exhibits the AlGaAs barriers (dark gray) and the InGaAs quantum well (light gray) between the barriers. The prewell, on the left-hand side of the barriers, can barely be seen due to the contrast between the layers.

Figure 1(b) presents the band structure, simulated at T = 4 K, according to the composition profile superposed on the microscopy image. The match between the structural dimensions and the simulation [30] indicates precisely controlled growth parameters. An accumulation region for electrons and a drift region for holes are present at the interface between GaAs and $Al_{0.2}Ga_{0.8}As$. The heterostructure doping profile is shown in Fig. 1(c). Lightly and highly doped regions are indicated by the symbols *n* and *n*++, respectively, and correspond to doping concentrations on the order of 10^{17} cm^{-3} and 10^{18} cm^{-3}. The buffer layer, which is closer to the substrate, is not present in this image range; therefore, it is indicated by an arrow, with the corresponding donor concentration.

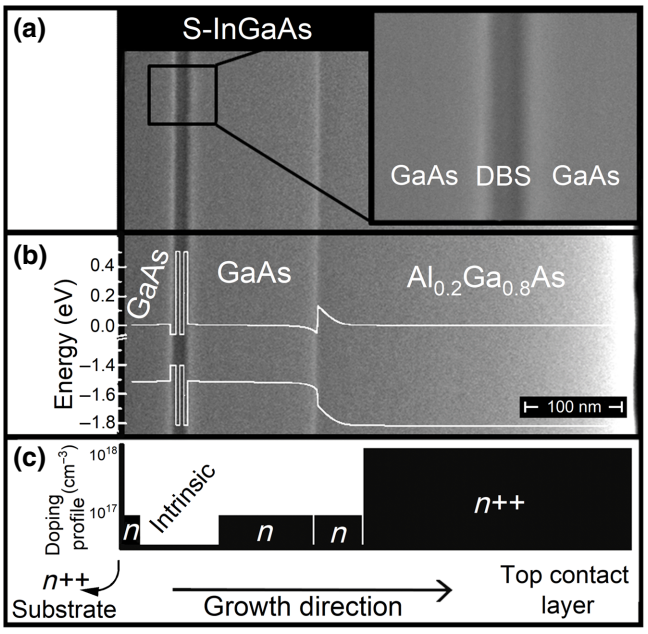

FIG. 1. (a) A cross-section SEM image of the S-InGaAs sample. An enlargement of the DBS is shown in the inset. (b) The band structure and (c) the doping profile of the S-InGaAs RTD.

B. Optical characterization

Electrical and optical measurements, with and without a magnetic field, are performed with the sample placed inside a helium closed-cycle cryostat with superconducting magnet coils (Attocube - Attodry1000) and the magnetic field oriented parallel to the growth direction. For each magnetic field value, a voltage sweep is performed and the EL signal and the current are measured. The experimental setup is displayed in Fig. 2. All measurements presented in this study are obtained at a nominal temperature of T = 4 K. The optical signal is collimated by an aspheric lens (NA = 0.64) and transmitted along a 50-μm multimode optical fiber, being dispersed by a 75-cm spectrometer and detected by a silicon CCD detector (Andor, Shamrock/iDus).

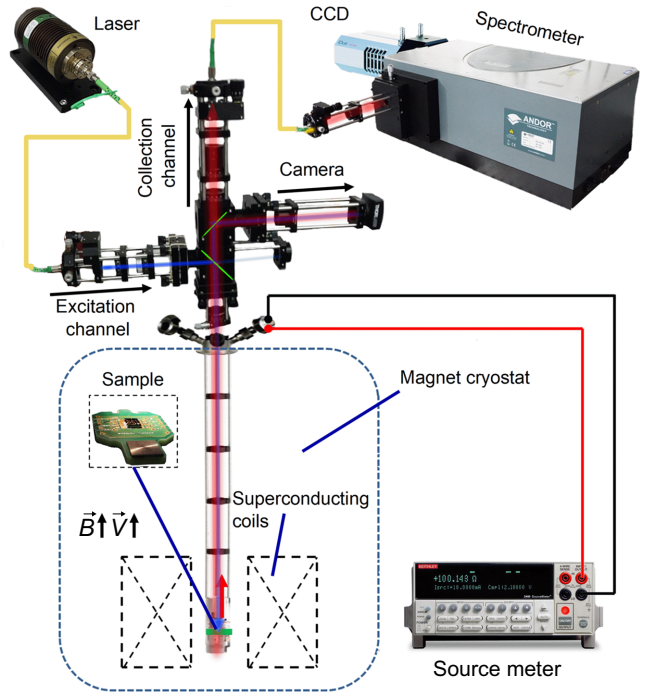

FIG. 2. The experimental setup for the EL and PL measurements (adapted from Ref. [31]).

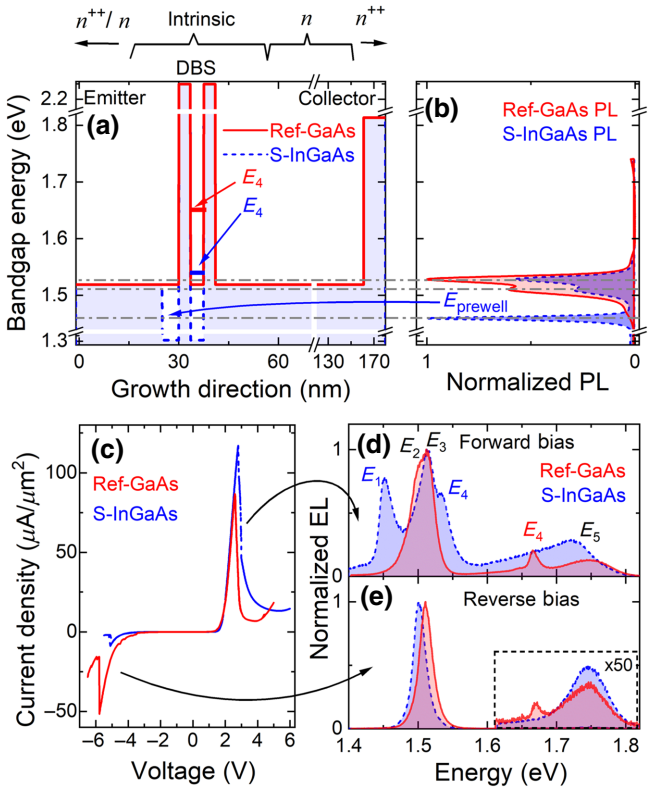

FIG. 3. (a) The band-gap energy profile of the S-InGaAs sample (blue dashed line) and of Ref-GaAs (red line). The bulk GaAs and donor levels are depicted as horizontal dashed lines. The DBQW confinement energies (E_4; see Table I) for Ref-GaAs and S-InGaAs are represented as red and blue lines, respectively. n and n^{++} indicate regions where the structure is lightly ($n \sim 10^{17}$) and highly ($n \sim 10^{18}$) doped, respectively. (b) The PL spectra obtained for each sample, in their respective colors. Both samples present two emission lines related to donor and bulk GaAs emissions. The S-InGaAs has an additional emission peak from the prewell. (c) The current-voltage (I-V) characteristics for the two samples. The arrows indicate the voltage biases where the EL signal is obtained at resonance. S-InGaAs (blue) and Ref-GaAs (red) EL spectra at (d) forward and (e) reverse bias voltages. Five emission lines are identified, from E_1 to E_5 (see Table I).

III. RESULTS AND DISCUSSION

A. Optical and electrical properties at zero magnetic field

The band-gap energy profiles at T = 4 K, of the two samples under study are shown in Fig. 3(a). The normalized PL spectra obtained at 4 K and without an applied voltage are presented in Fig. 3(b). For both samples, two emission lines are present, corresponding to the donor level [32,33] and the bulk GaAs recombination, labeled as E_2 and E_3 in Table I, respectively. The two emission lines are almost identical, which indicates that the growth details (except for the prewell and the quantum well) are nearly identical. For the S-InGaAs sample, the prewell emission (E_1 in Table I) can also be seen. Its emission line is more pronounced compared to the GaAs peak, with a peak height approximately 74% higher than E_3.

The current-density–voltage characteristics, $j(V)$, for Ref-GaAs and S-InGaAs, are presented in Fig. 3(c). For a forward bias voltage, the S-InGaAs (Ref-GaAs) peak current density is $j_{\rm res} = 117\ \mu{\rm A}/\mu{\rm m}^2$ ($j_{\rm res} = 87\ \mu{\rm A}/\mu{\rm m}^2$) at $V_{\rm res} = 2.8$ V ($V_{\rm res} = 2.6$ V) and the PVCR is 8.9 (12.8). As the heterostructure layouts (apart from the prewell and quantum well) are identical, the resonant currents and voltages are comparable. After the resonance voltage, the S-InGaAs valley current density comprises a wider voltage range with a minimum at $V = 5.3$ V, whereas the Ref-GaAs minimum valley current density is at $V = 3.8$ V. Moreover, the valley current density is higher for the S-InGaAs sample, leading to a lower PVCR at 4 K. At a reverse bias voltage, the S-InGaAs peak current density is $j_{\rm res} = -8.9\ \mu{\rm A}/\mu{\rm m}^2$ at $V_{\rm res} = -5.10$ V, while the Ref-GaAs peak current density is $j_{\rm res} = -51.6\ \mu{\rm A}/\mu{\rm m}^2$ at $V_{\rm res} = -5.78$ V. The heterostructure asymmetry leads to a reduction in the absolute value of the peak current density compared to forward bias and this reduction is more pronounced for the heterostructure containing the prewell (see Ref. [34]).

After surpassing a critical voltage of $V \geq 1.8$ V, the EL emission is observed [25]. To gain an accurate understanding of the origin of the EL, normalized EL spectra for both S-InGaAs and Ref-GaAs samples are obtained at resonant-current conditions (EL at $V = V_{\rm res}$) and are

TABLE I. The energy peak position of the emission lines for Ref-GaAs and S-InGaAs spectra measured via PL and EL [Figs. 3(b) and 3(d)]. The emissions are labeled as E_1 = InGaAs prewell, E_2 = donor GaAs, E_3 = bulk GaAs, E_4 = DBQW, and E_5 = bulk AlGaAs. All quantities are in electronvolts.

Sample	Technique	E_1	E_2	E_3	E_4	E_5
Ref-GaAs	PL	–	1.510	1.528	–	–
	EL	–	1.497	1.514	1.660	1.760
S-InGaAs	PL	1.460	1.510	1.529	–	–
	EL	1.452	1.496	1.514	1.534	1.740

shown in Figs. 3(d) and 3(e), for forward and reverse bias voltages, respectively. At forward bias, the S-InGaAs EL spectrum shows five main emission lines, according to Table I. In turn, the Ref-GaAs spectrum consists of four emission lines, without the lower energy peak ascribed to the prewell, as observed for the S-InGaAs sample. The emission lines E_1, E_2 and E_3 are lower in energy compared to the PL, probably due to the Joule heating. The DBQW emission energy E_4 differs between the two samples. With the EL measurements, we have access to the quantum-well states during the resonant tunneling while measuring the current-voltage (I-V) characteristics. It is not possible to observe the DBQW emission line through PL at $V = 0$ V, whereas in measuring PL with $V \neq 0$ V, the incident light can disturb the system and change the intrinsic charge-carrier dynamics and DBQW quantization due to the large photogeneration of electron-hole pairs [35–37]. For Ref-GaAs, we can extract the sum of the electron and hole quantization energies ($E_{e^-} + E_h = 146$ meV) by subtracting E_4 from E_3, whereas the same is not possible for S-InGaAs as we do not have optical information from the bottom of the InGaAs quantum well.

At reverse bias, both S-InGaAs and Ref-GaAs EL spectra present the GaAs and AlGaAs emission lines and the DBQW peak is visible only for the reference sample. Under reverse bias, electrons undergo impact ionization mostly in the highly doped GaAs layer on the substrate side. Generated holes drift through the DBS toward the top-contact side and accumulate at the interface between the GaAs and AlGaAs valence-band barrier. The presence of E_3 and the absence of donor emission, E_2, suggest that electron-hole recombinations are occurring along the lightly doped GaAs layer. A portion of the holes overcomes the barrier and reaches the optical window. The absence of InGaAs prewell emission at reverse bias indicates that the prewell is completely depleted of electrons.

The EL emission across the whole voltage range provides an insight into the internal charge-carrier transport processes as well as the evolution of the band profiles. S-InGaAs and Ref-GaAs normalized EL spectra for different voltage values are presented in Fig. 4(a).

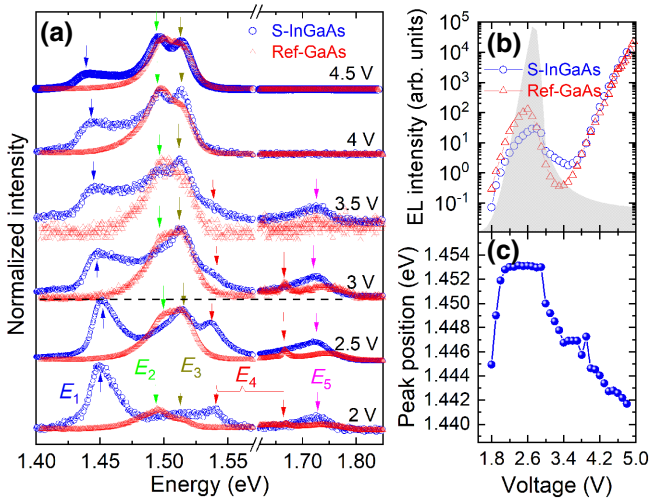

FIG. 4. (a) Normalized EL spectra for S-InGaAs (blue circles) and Ref-GaAs (red circles) for different bias voltages. Ref-GaAs emissions are normalized according to the maximum of S-InGaAs, disregarding the prewell emission. (b) The S-InGaAs (blue open circles) and Ref-GaAs (red open triangles) integrated intensity versus the bias voltage. A gray shadow of the S-InGaAs I-V characteristics is also plotted. (c) The prewell peak position as a function of the voltage (blue dots).

The calculated impact-ionization threshold is $E_{th}^{GaAs} = 1.80$ eV for the GaAs and $E_{th}^{AlGaAs} = 2.08$ eV for the AlGaAs optical window, obtained by considering energy and momentum conservation in the transitions during the ionization processes [28,38]. For both heterostructures, the onset for EL starts at $V = 1.8$ V due to E_{th}^{GaAs}. The AlGaAs peak, E_5, is present at voltages V > 2.0 V, which means that a fraction of the electrons travel ballistically through the drift region without impact ionization or scattering events before reaching the AlGaAs optical window and, as this region is not well defined, EL onset variations may occur. As the applied electric field increases, more holes are created at the optical window, increasing the intensity of the emission E_5. At higher bias voltages ($V > 3.5$ V), E_5 starts to vanish because generated holes in the AlGaAs region are swiped out toward the DBQW before they are able to recombine with electrons. The light emission from the DBQW, E_4, is also present at low bias voltages and increases up to the resonance condition as the quantum well gets populated. After the resonance voltage, E_4 emission drops abruptly because, in the off-resonance condition, the electron density inside the quantum well is significantly reduced [39].

At low bias voltages (2.0 V), the prewell emission, E_1, dominates. Holes created on the top-contact side drift toward the DBS and either recombine with electrons in the lightly doped [see Figs. 1(b) and 1(c)] or intrinsic GaAs region, DBQW, corresponding to the transitions E_3 and E_4, respectively, in Fig. 4(a) or tunnel through

the DBS. In this latter case, they are able to recombine with electrons in the prewell and with electrons in the highly doped GaAs region of the emitter side, leading to the emissions E_1 and E_2 at the low energy side of Fig. 4(a). On the other hand, as the Ref-GaAs does not have a prewell, the holes recombine mostly with electrons from GaAs layers. When the bias voltage is above resonance ($V \geq 3.0$ V), electron-charge buildup in the prewell is supported, which results in an increasing asymmetry of its EL emission (E_1). Furthermore, holes are more likely to be swiped into the highly doped region on the substrate side and recombine with electrons. Thus, the emission E_2 becomes more predominant compared to E_3.

The Ref-GaAs and S-InGaAs EL integrated intensity versus the voltage are shown in Fig. 4(b). A gray shadow of the S-InGaAs I-V characteristics is also plotted. The two intensity curves are comparable, with a peak at resonance, followed by an intensity drop in the valley region. At high voltages, the intensity increases again. Within the NDC region, the RTD without a prewell presents an EL-intensity decrease of almost 3 orders of magnitude. A one-order-of-magnitude reduction is observed for S-InGaAs. We have demonstrated, in a recent work, that the higher EL peak-to-valley ratio (PVR) for Ref-GaAs is due to competition between coherent and sequential tunneling channels [25]. The smaller optical PVR for the S-InGaAs heterostructure at cryogenic temperatures is probably caused by the prewell charge buildup. By analyzing the prewell peak position in Fig. 4(c), obtained at the peak maximum intensity, we observe an increase from 1.445 eV to 1.453 eV before 2.0 V and then it becomes nearly constant up to the resonant voltage due to electrostatic feedback, screening the prewell (see Refs. [14] and [15]). After the resonance, we can observe a constant red shift of the prewell energy of about -4.40 ± 0.24 meV/V.

In this section, we investigate the charge-carrier dynamics as function of the applied voltage, at $B = 0$ T, by analyzing the EL variations along the voltage range, and we address the differences between the structures with and without the emitter prewell. The next section is focused on the dependence of the electrical and optical properties on the magnetic field and the determination of the charge-carrier density by two different means.

B. Magnetic field dependence of EL and electric transport

Figures 5(a) and 5(b) present the two-dimensional (2D) intensity maps of the S-InGaAs EL spectra as a function of the applied magnetic field and voltage. The top and bottom panels correspond to measurements performed before and after the resonance current peak, respectively.

We can resolve a fanlike pattern of Landau levels (LLs) in the EL, spreading out from the emitter prewell emission line as the magnetic field increases over a wide voltage range. On the other hand, no LL splitting is observed for the DBQW state. LLs are also absent from the Ref-GaAs heterostructure (not shown). The differences in the LL splitting before and after the resonant condition are worth noting. At voltages up to resonance, we observe a picture in which the levels are not well resolved. This indicates that the quasi-Fermi energy at the prewell, E_F^{prewell}, is close to the prewell ground state. In this case, the DBQW is supporting a strong charge buildup due to resonant conditions and the electrons tunnel through the double

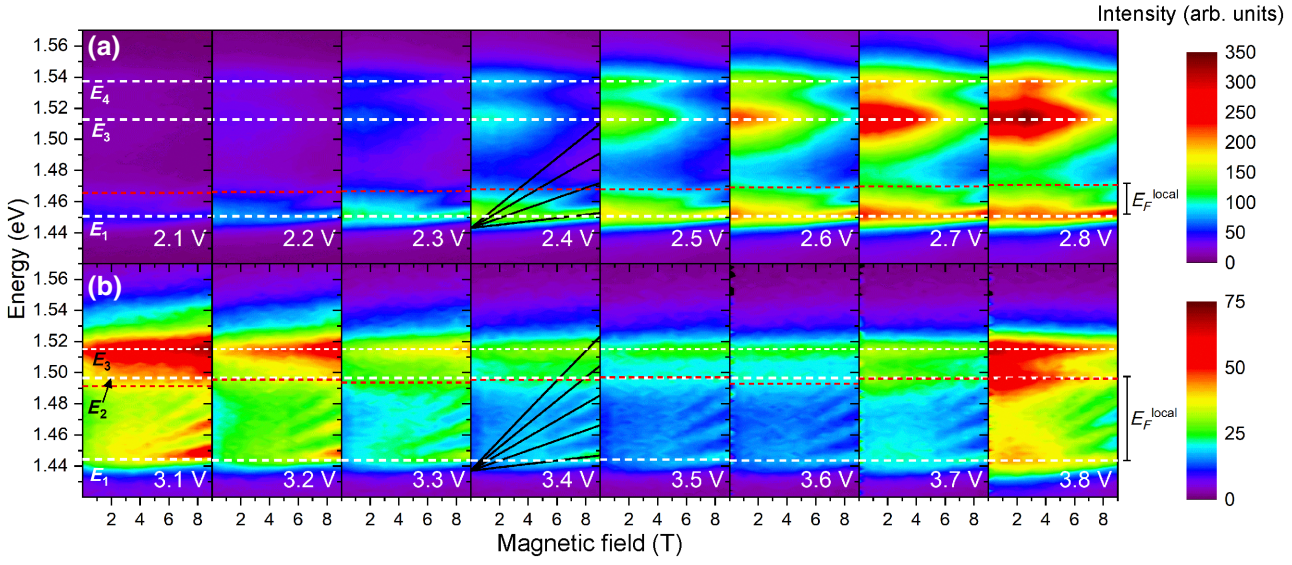

FIG. 5. The color map of the S-InGaAs EL signal versus the magnetic field for voltages (a) before (upper panels) and (b) after resonance (lower panels). The black lines in the middle graphs indicate the Landau-level splitting calculated using Eq. (1).

barrier rather than accumulating in the prewell. In the off-resonance case, the energy-level misalignment quenches the resonant-tunneling rate and electrons accumulate in the prewell, raising E_F^{prewell} at higher energies [40].

A peculiar feature is also observed at voltages from 3.1 V to 3.5 V [Fig. 5(b)], where the EL intensity tends to increase with the magnetic field, whereas at voltages below and above this voltage range, the opposite occurs. The Ref-GaAs structure EL intensity at this voltage (not shown) also increases with the magnetic field.

From the experimental dependencies of the transition energies on the magnetic field, we calculate the energy separation of the LLs using a two-band model [41,42]. In this model, the energies of the Landau transitions between a parabolic band for the holes and the nonparabolic band for the electrons are given by

$$E_N = \frac{E_g}{2} + \sqrt{\left(\frac{E_g}{2} + E_0\right)^2 + E_g\left(N + \frac{1}{2}\right)\frac{\hbar e B}{m_{0,e}}} + \left(N + \frac{1}{2}\right)\frac{\hbar e B}{m_{0,h}} + H_0, \quad (1)$$

where $m_{0,e} = 0.071 m_0$ [43] and $m_{0,h} = 0.15 m_0$ [44] are the effective masses of the $In_{0.15}Ga_{0.85}As$ conduction and valence bands, respectively; E_g is the band-gap energy of the $In_{0.15}Ga_{0.85}As$ prewell; N is the Landau-level quantum number; and E_0 and H_0 are the electron and hole subband energies. The calculation results are shown as solid lines in the color plots of Fig. 5 at 2.4 V and 3.4 V, where it can be seen that all Landau energies fit well with the experiment.

Figure 6(a) shows the current-density characteristics taken at zero magnetic field (dashed lines) and $B = 9$ T (solid lines) for Ref-GaAs and S-InGaAs, colored red and blue, respectively. The S-InGaAs (Ref-GaAs) resonance-current-density peak decreases from 117 μA/μm^2 (93 μA/μm^2) to 105 μA/μm^2 (74 μA/μm^2) and shifts from 2.80 V (2.95 V) to 3.05 V (3.03 V) by sweeping the magnetic field from 0 to 9 T. The PVCR decreases from 8.9 (14.2) to 8.5 (11.2), driven by the reduction in the peak current density. At $V = 3.2$ V, a small shoulder in the current density is observed, as shown in the insets of Fig. 6(a). Figures 6(b) and 6(c) present the current-density difference between transport measurements with and without an applied magnetic field (from 1 T to 9 T) in the range between 3.08 and 3.40 V, for Ref-GaAs and S-InGaAs, respectively. Note that a current-density peak emerges and changes position with the magnetic field and that there is a correlation with the EL-intensity increase between 3.1 V and 3.5 V observed in Fig. 5(b). The increased current density with the magnetic field leads to a higher hole-generation rate and, therefore, the luminescent signal increases. It is important to note that the light-emission increase and the current-density increase with the magnetic field are not proportional. This is because the

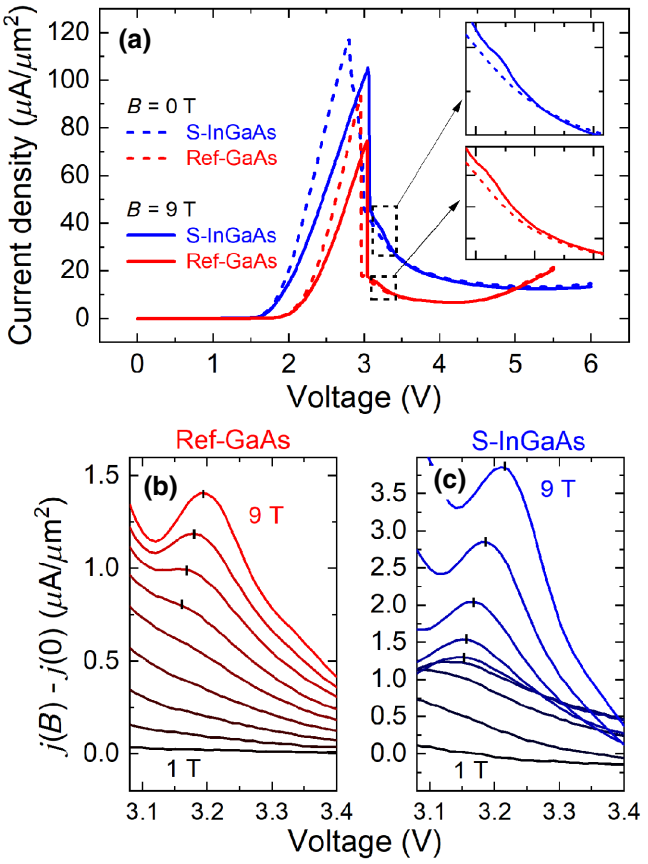

FIG. 6. (a) The I-V characteristics for Ref-GaAs (red) and S-InGaAs (blue), obtained at $B = 0$ T (dashed lines) and 9 T (solid lines). The insets represent enlargements of the voltage range between 3.0 V and 3.8 V. A small shoulder is observed around 3.2 V. The current-density difference between curves with an applied magnetic field $[j(B) - j(0)]$, for (b) Ref-GaAs and (c) S-InGaAs, from 3.08 V to 3.40 V.

hole-generation rate is enhanced when the system is in the on-resonance regime [25]. This feature is evidence of the LL quantization from the DBQW in resonance with the prewell ground state as described in Refs. [45–47].

We can extract relevant quantitative information on the charge accumulation by combining both the transport and optical results under a magnetic field. First, we focus on the current versus the magnetic field, from which we can estimate the charge-carrier density at the prewell [13,40]. From the S-InGaAs (Ref-GaAs) I-V characteristics at several magnetic fields, the normalized current oscillations are plotted as a function of the inverse field, $1/B$, as blue (red) lines, presented in Fig. 7(a). We measure the I-V characteristics at several magnetic field values and then extract the current as a function of the magnetic field by transposing the data and fixing the voltage. Oscillations are visible in both samples and are the signature of 2D-electron-gas (2DEG) quantization due to the crossing of the Landau levels and the Fermi energy [40]. In the S-InGaAs case, these oscillations are produced by the InGaAs emitter prewell

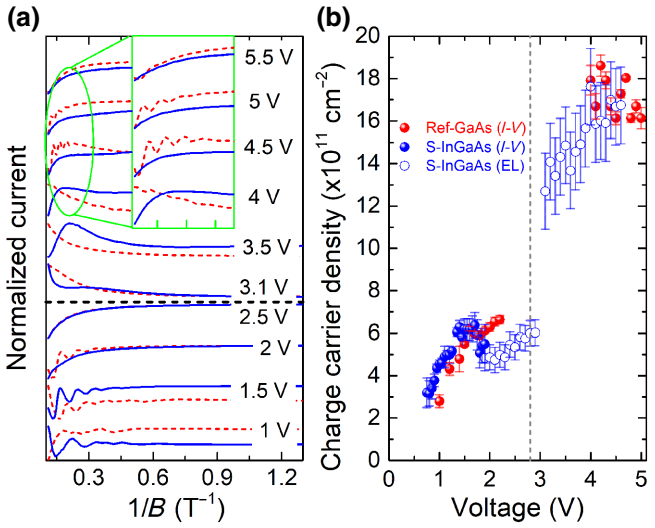

FIG. 7. (a) The normalized current oscillations as a function of the magnetic field for several bias-voltage values from 1.0 V up to 5.5 V for S-InGaAs (blue lines) and Ref-GaAs (red lines), offset for clarity. Voltages before (after) the resonance condition are located below (above) the horizontal dashed line. The inset shows an enlargement for 4.0 V up to 5.5 V. (b) The charge-carrier density as a function of the voltage extracted from the EL emission for S-InGaAs (open blue circles) and from the current oscillations, for S-InGaAs and Ref-GaAs, in blue and red dots, respectively. The vertical dashed line refers to the resonance voltage.

Landau quantization and they can be resolved from 0.75 V to 1.95 V, after which they can no longer be resolved. For the Ref-GaAs sample, an emitter triangular prewell is formed due to the band structure bending with the electric field [48]. The oscillations are present from 1 V to 2.2 V and can be further seen after the resonance, presenting a higher frequency, from 4 V and onward.

Figure 7(b) displays the charge-carrier density inside the (triangular) emitter prewell (η_{prewell}) as a function of the voltage for the S-InGaAs (Ref-GaAs) obtained through the current oscillations with period $\Delta(1/B)$ [13,16,17] as

$$\eta_{\text{prewell}} = \frac{e}{\hbar\pi\,\Delta(1/B)}. \tag{2}$$

Note that, before resonance, the calculated charge-carrier densities in the two samples are similar, as they are grown using the same donor profile. In the off-resonance case, the charge-carrier density can be calculated for Ref-GaAs after 4 V and is observed to be higher than for the on-resonance condition due to charge buildup at the emitter barrier [40]. It is not possible, however, to calculate the charge-carrier density for voltages above resonance for the S-InGaAs sample using magneto-transport measurements, since the oscillations are not observed. The lack of current oscillation after resonance is probably due to incoherent transport, such as sidewall leakage, thermionic emission, and incoherent tunneling, which are not influenced by the magnetic field. For the Ref-GaAs, the oscillations observed from 4 V indicate coherent transport, which can be associated with tunneling through excited DBQW levels. The S-InGaAs coherent-transport current oscillations would appear after 6 V, beyond the experimental voltage range. Nevertheless, in this scenario, EL measurements can be useful for the charge-buildup investigation and they complete the map of the carrier-density changes throughout the full operation range of the device. By considering that the charge carriers are thermalized, we can calculate the density of the 2D states at the prewell as follows [13,16,17]

$$\eta_{\text{prewell}} = \frac{E_F^{\text{prewell}} m^*}{\hbar^2\pi}. \tag{3}$$

By analyzing the prewell emission, E_1, before resonance [Fig. 5(a)], we can define the prewell quasi-Fermi energy, E_F^{prewell}, as the difference between the peak position and the energy at half maximum, at $B = 0$ T [49,50]. After resonance, as shown in Fig. 5(b), the prewell emission asymmetry interferes with the donor emission line, E_2, making it difficult to determine the quasi-Fermi energy using prior procedure. We thus develop an alternative method. By analyzing the EL intensity as a function of the magnetic field for fixed energy values, the Landau-level oscillations are clearly resolved. Thus, we determine E_F^{prewell} as the difference between E_1 and the energy position at which oscillations are no longer detected and extrapolate it down to 0 T.

The charge-carrier density extracted from the EL measurements using that method is depicted in Fig. 7(b) as open blue circles. The error bars before and after the resonance are estimated considering, respectively, the spectral noise and the donor emission line width due to the interference between the LLs and E_2. As one can see, before resonance these results coincide within the same range of the blue dots and after resonance we obtain a charge-carrier density similar to that of the Ref-GaAs sample. These agreements are indications that the optical emission can also be used to estimate these quantitative features.

IV. CONCLUSIONS

In summary, we investigate the carrier dynamics of a GaAs/AlGaAs resonant-tunneling diode with an InGaAs emitter prewell and a quantum well, combining transport measurements and EL. A conventional GaAs/AlGaAs RTD is used as a reference sample, to further study the effects of the S-InGaAs heterostructure.

The magneto-transport results resemble what has already been reported in the literature. Before the resonant voltage, the charge-carrier densities obtained for the two

samples through the current magneto-oscillations are comparable; however, the lack of clear oscillations after resonance for the S-InGaAs sample prevents the determination of this parameter. We thus propose an approach to assess the charge accumulation through magneto-EL where the magneto-transport means are no longer effective. Internal charge-carrier transport processes are observed without the need for PL. This is known to be relevant for RTDs since their transport characteristics can be very sensitive to illumination. Furthermore, Landau-level quantization in the emitter prewell of a resonant-tunneling diode via EL is identified. The spreading of the LLs allows us to estimate the quasi-Fermi energy at the prewell and, thus, the charge-carrier density. The results show good agreement with the transport measurements in the operational range when they are both available. This method of combining complementary transport and optical tools for determining the charge-carrier buildup, which controls the operation of photodetectors, might pave the way for the development of potentially more efficient devices.

ACKNOWLEDGMENTS

We gratefully acknowledge the financial support of the following agencies: the Fundação de Amparo à Pesquisa do Estado de São Paulo (FAPESP) (Grants No. 2013/18719-1, No. 2014/19142-1, No. 2014/02112-3, and No. 2018/01914-0), the Conselho Nacional de Desenvolvimento Científico e Tecnológico (CNPq) (Grants No. 163785/2018-0 and No. 471191/2013-2), the Coordenação de Aperfeiçoamento de Pessoal de Nível Superior (CAPES) (Grant No. 88881.133567/2016-01), Bayerisches Hochschulzentrum für Lateinamerika (BAYLAT), and the German Federal Ministry of Education and Research (BMBF) within the national projects Hochsensitive Infrarotdetektoren auf Basis von Resonanz-Tunneldioden mit Halbleitern schmaler Bandlücke (HIRT) (Grant No. 13XP5003B) and Photon-N (Grant No. FKZ 13N15125).

[1] R. Tsu and L. Esaki, Tunneling in a finite superlattice, Appl. Phys. Lett. **22**, 562 (1973).

[2] L. L. Chang, L. Esaki, and R. Tsu, Resonant tunneling in semiconductor double barriers, Appl. Phys. Lett. **24**, 593 (1974).

[3] Jian Ping Sun, G. I. Haddad, P. Mazumder, and J. N. Schulman, Resonant tunneling diodes: Models and properties, Proc. IEEE **86**, 641 (1998)..

[4] M. Feiginov, H. Kanaya, S. Suzuki, and M. Asada, Operation of resonant-tunneling diodes with strong back injection from the collector at frequencies up to 1.46 tHz, Appl. Phys. Lett. **104**, 243509 (2014).

[5] M. Feiginov, Frequency limitations of resonant-tunnelling diodes in sub-tHz and tHz oscillators and detectors, J. Infrared Millim. Terahertz Waves **40**, 365 (2019).

[6] T. A. Growden, E. R. Brown, W. Zhang, R. Droopad, and P. R. Berger, Experimental determination of quantum-well lifetime effect on large-signal resonant tunneling diode switching time, Appl. Phys. Lett. **107**, 153506 (2015).

[7] R. T. Siewe, Response of a resonant tunnelling diode optoelectronic oscillator coupled to a non-linear electrical circuit, IET Optoelectronics **10**, 205 (2016).

[8] C. Ironside, B. Romeira, and J. Figueiredo, *Resonant Tunneling Diode Photonics* (Morgan & Claypool Publishers, San Rafael, 2019), p. 2053.

[9] F. Hartmann, F. Langer, D. Bisping, A. Musterer, S. Höfling, M. Kamp, A. Forchel, and L. Worschech, GaAs/AlGaAs resonant tunneling diodes with a GaInNaS absorption layer for telecommunication light sensing, Appl. Phys. Lett. **100**, 172113 (2012).

[10] A. Pfenning, F. Hartmann, F. Langer, M. Kamp, S. Höfling, and L. Worschech, Sensitivity of resonant tunneling diode photodetectors, Nanotechnology **27**, 355202 (2016).

[11] B. Nie, J. Huang, C. Zhao, W. Huang, Y. Zhang, Y. Cao, and W. Ma, InAs/GaSb superlattice resonant tunneling diode photodetector with InAs/AlSb double barrier structure, Appl. Phys. Lett. **114**, 053509 (2019).

[12] M. Ahmadzadeh, A. Ghadimi, and S. A. Sedigh Ziabari, External quantum efficiency of a resonant tunneling diode photo detector: Structural parameters and wavelength dependencies, Optik **221**, 165265 (2020).

[13] L. Eaves, M. Leadbeater, D. Hayes, E. Alves, F. Sheard, G. Toombs, P. Simmonds, M. Skolnick, M. Henini, and O. Hughes, Electrical and spectroscopic studies of space-charged buildup, energy relaxation and magnetically enhanced bistability in resonant-tunneling structures, Solid-State Electron. **32**, 1101 (1989).

[14] T. A. Fisher, P. D. Buckle, P. E. Simmonds, R. J. Teissier, M. S. Skolnick, C. R. H. White, D. M. Whittaker, L. Eaves, B. Usher, P. C. Kemeny, R. Grey, G. Hill, and M. A. Pate, Use of a narrow-gap prewell for the optical study of charge buildup and the Fermi-energy edge singularity in a double-barrier resonant-tunneling structure, Phys. Rev. B **50**, 18469 (1994).

[15] M. L. Leadbeater and L. Eaves, Sequential tunnelling and magnetically enhanced bistability in double barrier resonant-tunnelling structures, Phys. Scr. **T35**, 215 (1991).

[16] L. Eaves, G. A. Toombs, F. W. Sheard, C. A. Payling, M. L. Leadbeater, E. S. Alves, T. J. Foster, P. E. Simmonds, M. Henini, O. H. Hughes, J. C. Portal, G. Hill, and M. A. Pate, Sequential tunneling due to intersubband scattering in double-barrier resonant tunneling devices, Appl. Phys. Lett. **52**, 212 (1988).

[17] M. L. Leadbeater, E. S. Alves, F. W. Sheard, L. Eaves, M. Henini, O. H. Hughes, and G. A. Toombs, Observation of space-charge bulk-up and thermalisation in an asymmetric double-barrier resonant tunnelling structure, J. Phys.: Condens. Matter **1**, 10605 (1989).

[18] H. Riechert, D. Bernklau, J.. Reithmaier, and R. D. Schnell, High performance resonant tunnelling structures on GaAs substrates, Electron. Lett. **26**, 340 (1990).

[19] Y. W. Choi and C. R. Wie, Increased peak current in AlAs/GaAs resonant tunneling structures with GaInAs emitter spacer, J. Appl. Phys. **71**, 1853 (1992).

[20] T. B. Boykin, R. C. Bowen, G. Klimeck, and K. L. Lear, Resonant-tunneling diodes with emitter prewells, Appl. Phys. Lett. **75**, 1302 (1999).

[21] R. M. Lewis, H. P. Wei, S. Y. Lin, and J. F. Klem, Effects of prewells on transport in *p*-type resonant tunneling diodes, Appl. Phys. Lett. **77**, 2722 (2000).

[22] A. Pfenning, G. Knebl, F. Hartmann, R. Weih, A. Bader, M. Emmerling, M. Kamp, S. Höfling, and L. Worschech, Room temperature operation of GaSb-based resonant tunneling diodes by prewell injection, Appl. Phys. Lett. **110**, 033507 (2017).

[23] A. Pfenning, G. Knebl, F. Hartmann, R. Weih, M. Meyer, A. Bader, M. Emmerling, L. Worschech, and S. Höfling, GaSb/AlAsSb resonant tunneling diodes with GaAsSb emitter prewells, Appl. Phys. Lett. **111**, 171104 (2017).

[24] Y. Galvão Gobato, H. V. A. Galeti, L. F. dos Santos, V. López-Richard, D. F. Cesar, G. E. Marques, M. J. S. P. Brasil, M. Orlita, J. Kunc, D. K. Maude, M. Henini, and R. J. Airey, Spin injection from two-dimensional electron and hole gases in resonant tunneling diodes, Appl. Phys. Lett. **99**, 233507 (2011).

[25] E. R. Cardozo de Oliveira, A. Pfenning, E. D. Guarin Castro, M. D. Teodoro, E. C. dos Santos, V. Lopez-Richard, G. E. Marques, L. Worschech, F. Hartmann, and S. Höfling, Electroluminescence on-off ratio control of *n-i-n* GaAs/AlGaAs-based resonant tunneling structures, Phys. Rev. B **98**, 075302 (2018).

[26] A. Pfenning, F. Hartmann, M. Rebello Sousa Dias, L. K. Castelano, C. Süßmeier, F. Langer, S. Höfling, M. Kamp, G. E. Marques, L. Worschech, and V. Lopez-Richard, Nanothermometer based on resonant tunneling diodes: From cryogenic to room temperatures, ACS Nano **9**, 6271 (2015), pMID: 26035628.

[27] C. R. H. White, M. S. Skolnick, L. Eaves, and M. L. Leadbeater, Electroluminescence and impact ionization phenomena in a double-barrier resonant tunneling structure, Appl. Phys. Lett. **58**, 1164 (1991).

[28] F. Hartmann, A. Pfenning, M. Rebello Sousa Dias, F. Langer, S. Höfling, M. Kamp, L. Worschech, L. K. Castelano, G. E. Marques, and V. Lopez-Richard, Temperature tuning from direct to inverted bistable electroluminescence in resonant tunneling diodes, J. Appl. Phys. **122**, 154502 (2017).

[29] T. A. Growden, W. Zhang, E. R. Brown, D. F. Storm, D. J. Meyer, and P. R. Berger, Near-uv electroluminescence in unipolar-doped, bipolar-tunneling GaN/AlN heterostructures, Light: Sci. Appl. **7**, 17150 (2018).

[30] S. Birner, T. Zibold, T. Andlauer, T. Kubis, M. Sabathil, A. Trellakis, and P. Vogl, IEEE Trans. Electron Devices **54**, 2137 (2007).

[31] E. R. Cardozo de Oliveira, Ph.D. thesis, Federal University of São Carlos, Universidade Federal de Sao Carlos, Programa de Pos-graduacao em Fisica, 2019, https://repositorio.ufscar.br/handle/ufscar/11602.

[32] E. H. Bogardus and H. B. Bebb, Bound-exciton, free-exciton, band-acceptor, donor-acceptor, and auger recombination in gaas, Phys. Rev. **176**, 993 (1968).

[33] J. Wagner and M. Ramsteiner, Binding energies of shallow donors in semi-insulating gaas, J. Appl. Phys. **62**, 2148 (1987).

[34] J.-H. Lee, M. Shin, S.-J. Byun, and W. Kim, Wigner transport simulation of resonant tunneling diodes with auxiliary quantum wells, J. Korean Phys. Soc. **72**, 622 (2018).

[35] H. B. de Carvalho, M. J. S. P. Brasil, V. Lopez-Richard, Y. Galvão Gobato, G. E. Marques, I. Camps, L. C. O. Dacal, M. Henini, L. Eaves, and G. Hill, Electric-field inversion asymmetry: Rashba and stark effects for holes in resonant tunneling devices, Phys. Rev. B **74**, 041305(R) (2006).

[36] L. F. dos Santos, Y. Galvão Gobato, V. Lopez-Richard, G. E. Marques, M. J. S. P. Brasil, M. Henini, and R. J. Airey, Polarization resolved luminescence in asymmetric *n*-type GaAs/AlGaAs resonant tunneling diodes, Appl. Phys. Lett. **92**, 143505 (2008).

[37] L. F. dos Santos, Y. G. Gobato, M. D. Teodoro, V. Lopez-Richard, G. E. Marques, M. J. S. P. Brasil, M. Orlita, J. Kunc, D. K. Maude, M. Henini, and R. J. Airey, Circular polarization in a non-magnetic resonant tunneling device, Nanoscale Res. Lett. **6**, 101 (2011).

[38] R. Redmer, J. R. Madureira, N. Fitzer, S. M. Goodnick, W. Schattke, and E. Schöll, Field effect on the impact ionization rate in semiconductors, J. Appl. Phys. **87**, 781 (2000).

[39] C. Van Hoof, J. Genoe, R. Mertens, G. Borghs, and E. Goovaerts, Electroluminescence from bipolar resonant tunneling diodes, Appl. Phys. Lett. **60**, 77 (1992).

[40] C. J. Goodings, H. Mizuta, and J. R. A. Cleaver, Electrical studies of charge build-up and phonon-assisted tunneling in double-barrier materials with very thick spacer layers, J. Appl. Phys. **75**, 2291 (1994).

[41] J. Maan, Y. Guldner, J. Vieren, P. Voisin, M. Voos, L. Chang, and L. Esaki, Three-dimensional character of semimetallic InAs-GaSb superlattices, Solid State Commun. **39**, 683 (1981).

[42] M. Potemski, J. Maan, K. Ploog, and G. Weimann, Properties of a dense quasi-two-dimensional electron-hole gas at high magnetic fields, Solid State Commun. **75**, 185 (1990).

[43] E. D. Jones, S. K. Lyo, I. J. Fritz, J. F. Klem, J. E. Schirber, C. P. Tigges, and T. J. Drummond, Determination of energy-band dispersion curves in strained-layer structures, Appl. Phys. Lett. **54**, 2227 (1989).

[44] K.-S. Lee, C.-D. Lee, Y. Kim, and S. K. Noh, Dependence of the heavy-hole exciton reduced mass on quantum-well size in InGaAs/GaAs heterostructures, Solid State Commun. **128**, 177 (2003).

[45] C. E. T. Gonçalves da Silva and E. E. Mendez, Resonant tunneling via Landau levels in GaAs-$Ga_{1-x}Al_xAs$ heterostructures, Phys. Rev. B **38**, 3994 (1988).

[46] Y. Galvao Gobato, J. M. Berroir, Y. Guldner, J. P. Vieren, F. Chevoir, and B. Vinter, Selection-rule breakdown in coherent resonant tunneling in a tilted magnetic field, Phys. Rev. B **44**, 13795 (1991).

[47] S. A. Brown, L. D. Macks, T. A. Fisher, and M. Emeny, Inter-Landau-level transitions near the threshold of 2D-2D tunneling, Phys. Rev. B **56**, 1967 (1997).

[48] E. Böckenhoff, K. v. Klitzing, and K. Ploog, Tunneling from accumulation layers in high magnetic fields, Phys. Rev. B **38**, 10120 (1988).

[49] M. Líbezny, S. C. Jain, J. Poortmans, M. Caymax, J. Nijs, R. Mertens, K. Werner, and P. Balk, Photoluminescence determination of the Fermi energy in heavily doped strained $Si_{1-x}Ge_x$ layers, Appl. Phys. Lett. **64**, 1953 (1994).

[50] N. Lee, K. Lee, C. Lee, J. Kim, H. Y. Park, D. Kwak, H. Lee, and H. Lim, Determination of conduction band tail and Fermi energy of heavily Si-doped GaAs by room-temperature photoluminescence, J. Appl. Phys. **78**, 3367 (1995).